(Preprint) AAS 21-296

ASTEROID LANDING WITH A SOLAR SAIL: LANDER DEPLOYMENT

Iain Moore[*], Colin R. McInnes[†] and Matteo Ceriotti[‡]

A critical phase of any mission which aims to interact with the surface of an asteroid is in landing. This can be done via landing of the main spacecraft, or by the deployment of separate landers. In this work, the spacecraft will be propelled by a solar sail. The solar sail is capable of delivering high energy missions, given the unlimited momentum available from the Sun. The performance of the sail is dependent on the area to mass ratio of the sail/spacecraft combination. The separation of a significant mass from the main spacecraft will result in a change in performance of the solar sail. This changing performance will affect the dynamics of the solar sail in the near-asteroid environment. This work will investigate the effects of the solar sail in the dynamics of the near asteroid space, as well as the instantaneous change of dynamics at lander separation. Then, work will show the deployment of a lander from various regions of the problem, providing a probability analysis of the success of the lander reaching the surface with a ballistic deployment from each region. Deployment from the region interior to the potential ridge line is found to have the greatest success.

INTRODUCTION

Asteroids are an integral part of future plans for human exploration of the solar system and off-world habitation. The resources contained in asteroids (eg. water, precious metals) are proposed to both fuel[1] human expansion into the solar system as well as provide materials for infrastructure. Asteroids also pose a threat to continued human presence on Earth with extinction level impact events being a real possibility in the long term. In order to understand more about their composition, there have been several successful missions to obtain samples from the surface of an asteroid.

Most recently, the Hayabusa 2 team at JAXA successfully received the long awaited samples from asteroid Ryugu. This mission saw the successful deployment of the MASCOT lander,[2] developed by DLR in Germany. NASA has also recently collected a sample from the surface of asteroid Bennu with the OSIRIS-REx mission.[3] This sample will be returned to the Earth in 2023. Previously, JAXA and NASA have successfully visited, sampled and observed asteroids with the Hayabusa[4] and NEAR-Shoemaker[5] missions respectively. ESA have also contributed in recent years with the Rosetta[6] mission to comet 67P/Churyumov-Gerasimenko where they deployed the Philae lander to the surface. There are also further missions in the pipeline, with NASA's NEA Scout,[7] the first solar sail mission to an asteroid. This mission will conduct a flyby of an asteroid, with the target body

[*]PhD Researcher, James Watt School of Engineering, University of Glasgow, University Avenue, Glasgow, G12 8QQ
[†]James Watt Chair, Professor of Engineering Science, James Watt School of Engineering, University of Glasgow, University Avenue, Glasgow, G12 8QQ
[‡]Lecturer in Space Systems Engineering, James Watt School of Engineering, University of Glasgow, University Avenue, Glasgow, G12 8QQ

dependent on the launch date and so the progress of the development of NASA's Space Launch System (SLS).

Crucial to these and future missions, is the successful deployment of landers to the asteroid surface. Deployment of a significant mass from a solar sail poses a unique challenge in that any change to the area to mass ratio of the sail/spacecraft combination will result in a change of sail performance. With the continuous acceleration provided by the sail, this changing performance has an inherent effect on the dynamics of the system.

In their work on mission design to the Trojan asteroids of Jupiter,[8] Farrés, Soldini and Tsuda present the two distinct phases of a solar power sail mission to an asteroid, deploying a lander to the surface. In this work, the two phases consist of the far-field dynamics for the sail monitoring of the lander after deployment, and the descent of the lander to the asteroid surface with focus on bouncing trajectories and ensuring the lander remains on the surface. This work demonstrates the unique ability of the sail to offer out-of-plane observation locations. However, the work shows these locations only in the Sun-asteroid 3-body system. These locations can be quite distant from the asteroid if the sail performance to asteroid gravitational parameter ratio is large. They do not take account of the points contained in the very near-asteroid region which result from the balance of the asteroid's gravitational, centrifugal and sail accelerations.[9,10] These points offer the same benefits as those of the 3-body system, but with the advantage of being contained in the asteroid rotational frame. Therefore, they present hover locations over the asteroid surface. Which are useful for continuous monitoring of a specific location from close to the surface.

Jiang *et al* have conducted research on the dynamics of the asteroid effective potential.[11–16] This work has shown the complex nature of the potential field of a rotating, highly irregular-shaped body, with a focus not only on the system equilibrium points, but also on periodic orbits around such points. There is also research on the effects of rotational velocity on the potential field. The body of work offers an extensive contribution to the study of such potential fields, with useful classification tools related to the stability of the equilibria. The work, however, only considers the natural system dynamics. The addition of a continuous thrust system (eg. solar sail, solar electric propulsion (SEP)) into the potential field brings a change. Yang *et al* present a study of the SEP case[17] and the effects on the dynamics of the system. However, the solar sail case is more complex still, given that the asteroid's rotation means that the sail dynamics are time-varying, owing to the apparent rotation of the Sun around the asteroid.

This work will present the changing dynamics of the asteroid potential field with the inclusion of a solar sail. Specifically, the work will present the time-varying, sail performance-varying and sail attitude varying dynamics around asteroid 4769 Castalia. The work will also consider the instantaneous change in sail performance, and resulting change in dynamics, at the point of separation of a MASCOT lander, deployed to the surface. Additionally, strategies for sail monitoring orbits and stationkeeping will be discussed. This work aims to add to the mission presented in previous work,[18] where the sail characteristic acceleration in the interplanetary phase is fixed at $a_c = 0.2$ mm/s^2.

Initially, the asteroid potential field is discussed and the chosen model for the asteroid is presented. Analysis of the phase space is then presented with discussion of equilibria and their stability, Zero Velocity Curves (ZVCs) and the theory of the potential ridge line.[19] Following this, the dynamics of the solar sail in the asteroid gravity field is presented. First, definitions of the sail attitude and performance parameter are discussed. Then, the effects of the constant acceleration

in the gravity field are shown with varying sail performance, attitude and solar position. Next, the instantaneous change in dynamics at the point of lander separation are discussed. Here, physical parameters for the sail and lander are presented and analysis of the effects of the changing dynamics is made. The next section presents four potential regions from which the lander can be deployed: equilibrium points, along the potential ridge line, interior to the ridge line and exterior to the ridge line. A probabilistic analysis is then conducted of the successful intersection with the surface by the lander, with zero-velocity release and a purely ballistic trajectory.

ASTEROID GRAVITY FIELD

Gravity model

For the purposes of demonstrating the theory and techniques discussed, this work uses the JPL polyhedron model of 4769 Castalia. The gravitational potential for a polyhedron is given by:[20]

$$U(\mathbf{r}) = \frac{1}{2} G\rho \left(\sum_{e \in \text{edges}} \mathbf{r}_e \cdot \mathbf{E}_e \cdot \mathbf{r}_e \cdot L_e - \sum_{f \in \text{faces}} \mathbf{r}_f \cdot \mathbf{F}_f \cdot \mathbf{r}_f \cdot \gamma_f \right) \tag{1}$$

where $\mathbf{E}_e$ is a dyad defined in terms of the face and edge normal vectors associated with each edge, L_e is a logarithmic term expressing the potential of a 1-D straight wire, $\mathbf{F}_f$ is a dyad defined for each face as the outer product of the face unit normal with itself and γ_f is the signed solid angle subtended by a face when viewed from the field point.[21]

The effective potential takes into account both the gravitational potential as well as the rotation of the asteroid, and is given by:[22]

$$V(\mathbf{r}) = \frac{1}{2}(\boldsymbol{\omega} \times \mathbf{r}) \cdot (\boldsymbol{\omega} \times \mathbf{r}) + U(\mathbf{r}) \tag{2}$$

where $\boldsymbol{\omega}$ is the vector of the rotational velocity of the asteroid and rotation is around the z-axis of the body fixed frame only. The Cartesian position of the particle relative to the body-fixed reference frame is given by $\mathbf{r}$. Asteroid 4769 Castalia has a density of $\rho = 2.1$ g/cm^3 and a rotational period of 4.095 hours.[11]

Phase space analysis

Although this work will focus on the dynamics of the asteroid system for a solar sail, it is informative to first analyse the phase space with no sail, before the sail is introduced later in the work.

Zero Velocity Curves The Zero Velocity Curves (ZVCs) represent boundaries which delimit accessible space based on the spacecraft's energy. The ZVCs are defined where the effective potential is equal in value to the Jacobi constant. The Jacobi constant is given by:[11]

$$C = \frac{1}{2}\dot{\mathbf{r}} \cdot \dot{\mathbf{r}} + V(\mathbf{r}) \tag{3}$$

and the ZVCs are found where:[23]

$$C = V(\mathbf{r}) \tag{4}$$

Therefore, in 2-dimensions, the ZVCs are the contour lines of the effective potential.

Equilibrium points The equilibrium points of a system are the critical points of the effective potential.[11] Therefore, the equilibrium points are obtained where:

$$\nabla V(\mathbf{r}) = 0 \tag{5}$$

Stability of equilibrium points An important factor in the study of the dynamics in the near-asteroid regime is the stability of the equilibrium points. Such a study requires linearisation of the equations of motion around the equilibrium point. As such, the following transformations are made:

$$\begin{aligned} \xi &= x - x_L \\ \eta &= y - y_L \\ \zeta &= z - z_L \end{aligned} \tag{6}$$

where $(x_L, y_L, z_L)^T$ is the Cartesian position of the equilibrium point. The second derivative terms of the effective potential will be denoted as follows:

$$\begin{aligned} V_{xx} &= \left(\frac{\partial^2 V}{\partial x^2}\right)_L \quad V_{yy} = \left(\frac{\partial^2 V}{\partial y^2}\right)_L \quad V_{zz} = \left(\frac{\partial^2 V}{\partial z^2}\right)_L \\ V_{xy} &= \left(\frac{\partial^2 V}{\partial x \partial y}\right)_L \quad V_{yz} = \left(\frac{\partial^2 V}{\partial y \partial z}\right)_L \quad V_{xz} = \left(\frac{\partial^2 V}{\partial x \partial z}\right)_L \end{aligned} \tag{7}$$

The full equation of motion is given by:

$$\ddot{\mathbf{r}} + 2\omega \times \dot{\mathbf{r}} + \nabla V(\mathbf{r}) = 0 \tag{8}$$

Combining Eqs. 6 and 7 with Eq. 8, the linearised equations of motion relative to the equilibrium point can be written as:[11]

$$\begin{aligned} \ddot{\xi} - 2\omega\dot{\eta} + V_{xx}\xi + V_{xy}\eta + V_{xz}\zeta &= 0 \\ \ddot{\eta} + 2\omega\dot{\xi} + V_{xy}\xi + V_{yy}\eta + V_{yz}\zeta &= 0 \\ \ddot{\zeta} + V_{xz}\xi + V_{yz}\eta + V_{zz}\zeta &= 0 \end{aligned} \tag{9}$$

These equations can also be expressed in the form:

$$\mathbf{M}\ddot{\mathbf{X}} + \mathbf{G}\dot{\mathbf{X}} + \mathbf{K}\mathbf{X} = 0 \tag{10}$$

where:

$$\begin{aligned} \mathbf{X} &= [\xi, \eta, \zeta]^T \qquad \mathbf{M} = \begin{bmatrix} 1 & 0 & 0 \\ 0 & 1 & 0 \\ 0 & 0 & 1 \end{bmatrix} \\ \mathbf{G} &= \begin{bmatrix} 0 & -2\omega & 0 \\ 2\omega & 0 & 0 \\ 0 & 0 & 0 \end{bmatrix} \quad \mathbf{K} = \begin{bmatrix} V_{xx} & V_{xy} & V_{xz} \\ V_{yx} & V_{yy} & V_{yz} \\ V_{zx} & V_{zy} & V_{zz} \end{bmatrix} \end{aligned} \tag{11}$$

It should also be noted that $V_{xz} = V_{zx}$, $V_{yz} = V_{zy}$ and $V_{xy} = V_{yx}$. The eigenvalues, λ, can then obtained from the Jacobian matrix:

$$\mathbf{A} = \begin{bmatrix} \mathbf{0} & \mathbf{M} \\ \mathbf{K} & -\mathbf{G} \end{bmatrix} \tag{12}$$

The stability of the equilibrium point is defined by the nature of the eigenvalues, and these are divided into 5 classes,[11,24] which are shown here in Table 1.

Table 1: Classification of non-degenerate and non-resonant equilibrium points, taken from.[24] In stability, LS = linearly stable and U = unstable.

Case	Eigenvalues	Stability	No. of periodic orbits
1	$\pm ib_j \, (b_j \in \mathbf{R}^+; j = 1, 2, 3)$	LS	3
2	$\pm a_j \, (a_j \in \mathbf{R}^+; j = 1) \, , \pm ib_j \, (b_j \in \mathbf{R}^+; j = 1, 2)$	U	2
3	$\pm a_j \, (a_j \in \mathbf{R}^+; j = 1, 2) \, , \pm ib_j \, (b_j \in \mathbf{R}^+; j = 1)$	U	1
4a	$\pm a_j \, (a_j \in \mathbf{R}^+; j = 1) \, , \pm c \pm id \, (c, d \in \mathbf{R}^+)$	U	0
4b	$\pm a_j \, (a_j \in \mathbf{R}^+; j = 1, 2, 3)$	U	0
5	$\pm c \pm id \, (c, d \in \mathbf{R}^+) \, , \pm ib_j \, (b_j \in \mathbf{R}^+; j = 1)$	U	1

Fig. 1 shows the equilibrium points and ZVCs for asteroid Castalia.

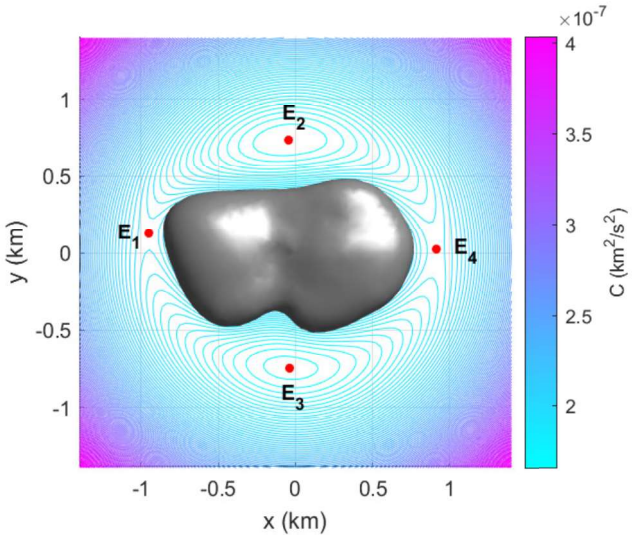

Figure 1: Zero velocity curves with equilibrium points represented by red dots for asteroid 4769 Castalia

Table 2 shows the Cartesian position of each equilibrium point and Tab. 3 shows the respective eigenvalues.

The potential ridge line The potential ridge line is presented by Tardival in his PhD thesis as well as subsequent publications.[19,25] This ridge line represents the locus of points where the gradient of the potential is close to zero, necessarily including the equilibrium points. A simple algorithm for

Table 2: Position of equilibrium points in the effective potential field of asteroid 4769 Castalia

	x (km)	y (km)	z (km)
E_1	-0.953	0.129	0.030
E_2	-0.043	0.736	0.003
E_3	-0.040	-0.744	0.009
E_4	0.910	0.023	0.034

Table 3: Eigenvalues for equilibrium points in effective potential field of asteroid 4769 Castalia

	λ_1	λ_2	λ_3	λ_4	λ_5	λ_6	Case	Stability
E_1	-0.0005	0.0005	0.0006i	-0.0006i	0.0006i	-0.0006i	2	U
E_2	0.0002 + 0.0004i	0.0002 - 0.0004i	-0.0002 + 0.0004i	-0.0002 - 0.0004i	0.0004i	-0.0004i	5	U
E_3	-0.0002 + 0.0004i	-0.0002 - 0.0004i	0.0002 + 0.0004i	0.0002 - 0.0004i	0.0004i	-0.0004i	5	U
E_4	0.0004	-0.0004	0.0006i	-0.0006i	0.0005i	-0.0005i	2	U

the calculation of the ridge line[26] is provided in which the method of bisection allows for rapid calculation of the point of zero acceleration along the primary calculation axis. In this work, the primary calculation axis is chosen to be the x-axis. In order to simplify the process, the asteroid is rotated through one full revolution such that calculation is required in the x-z plane only. Figure 2 shows the ridge line and natural equilibrium points for asteroid 4769 Castalia.

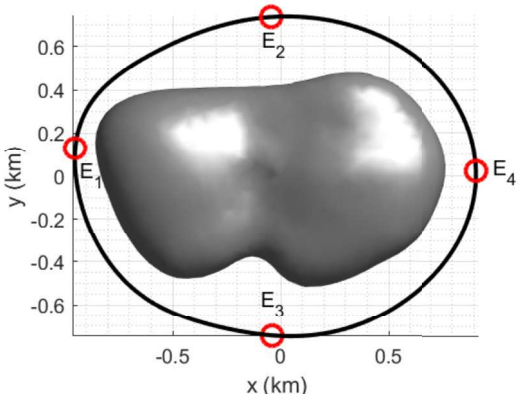

Figure 2: Potential ridge line for asteroid 4769 Castalia. Equilibrium points shown in red circles.

SOLAR SAIL DYNAMICS

Solar sails are a very thin, highly reflective membrane which can offer propellantless propulsion for spacecraft. They operate by a transfer of momentum from photons, radiated by the Sun, to the sail. The sail attitude is defined by two parameters in this work; the cone (α) and clock (δ) angles. Figure 3 shows how these angles are defined, where $\hat{\mathbf{p}}$ is the normal to the orbit plane.

The acceleration provided by the solar sail is given by:[27]

$$\mathbf{a}_{SS} = a_c \left(\hat{\mathbf{r}}_{sun} \cdot \hat{\mathbf{n}}\right)^2 \hat{\mathbf{n}} \tag{13}$$

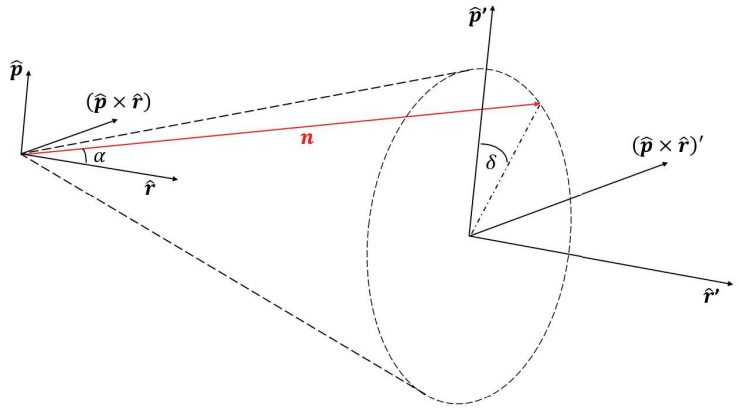

Figure 3: Definition of cone (α) and clock (δ) angles.

where $\hat{\mathbf{r}}_{sun}$ is the unit vector of the Sun-sail line and $\hat{\mathbf{n}}$ is the sail normal unit vector, given by:[27]

$$\hat{\mathbf{n}} = [\cos\alpha, \sin\alpha\sin\delta, \sin\alpha\cos\delta]^T \tag{14}$$

As the acceleration of the sail is given by the gradient of the potential, the potential of the sail can be given by:[17]

$$V_{SS}(\mathbf{r}) = \mathbf{a}_{SS}\cdot\mathbf{r} \tag{15}$$

and so the total effective potential of the sail in the potential field of the asteroid is given by:

$$V_{total}(\mathbf{r}) = \frac{1}{2}(\boldsymbol{\omega}\times\mathbf{r})\cdot(\boldsymbol{\omega}\times\mathbf{r}) + U(\mathbf{r}) + V_{SS}(\mathbf{r}) \tag{16}$$

The equation of motion for a solar sail in the potential field of a uniformly rotating asteroid is therefore given by:

$$\ddot{\mathbf{r}} + 2\omega\times\dot{\mathbf{r}} - \nabla V_{total}(\mathbf{r}) = 0 \tag{17}$$

As the asteroid is rotating with a period of 4.095 hours, in the body-fixed frame, the Sun will appear to orbit around the asteroid, in the x-y plane with this same period. As such, the unit vector of the Sun-sail line is given by:[28]

$$\hat{\mathbf{r}}_{sun} = [\cos\omega t, -\sin\omega t, 0]^T \tag{18}$$

At the initial time, t_0, the Sun-sail unit vector is $\hat{\mathbf{r}}_{sun} = [1,0,0]^T$.

EFFECTS OF THE SOLAR SAIL ON SYSTEM DYNAMICS

Artificial Equilibrium Points (AEPs)

By varying the attitude and performance of the sail, the position of the equilibrium points can be artificially displaced. These new equilibrium points are referred to as Artificial Equilibrium Points

(AEPs).[17] For clarity, the notation of the AEPs will be AEP_n and the natural equilibrium points will maintain the form E_n. The range of variation in the position of the AEP for varying sail attitude is limited by the sail performance.[10]

Effects of sail performance on AEPs When the sail is introduced to the dynamics of the system, the additional constant acceleration causes a change in the structure of the zero velocity curves and the position of the equilibrium points.[17] Figure 4 shows how the changing performance of the sail displaces the equilibria when time is frozen at t_0. In this example, the sail attitude is set with $\alpha = \delta = 0^\circ$ and the sail performance is varied in the range $a_c \in [0, 0.4]$ mm/s^2. AEP_1 and AEP_2 vanish at the critical performance value of approximately $a_c = 0.06$ mm/s^2. AEP_3 moves in the negative x-direction while AEP_4 descends towards the surface of the asteroid where it will eventually collide, and vanish, with the internal equilibrium point of Castalia at $a_c = 0.20$ mm/s^2.

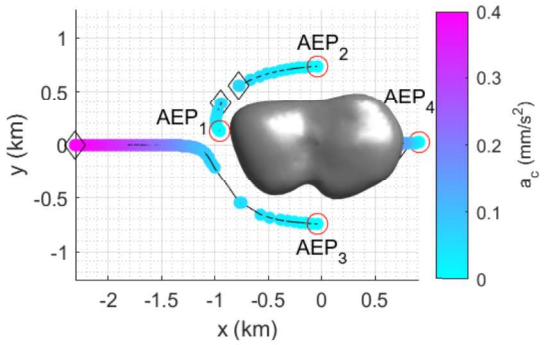

Figure 4: Motion of the equilibria for $\alpha = \delta = 0^\circ$ and $a_c \in [0, 0.4]$ mm/s^2. Red circle represents initial point and black diamond represents end points, with the black line tracing the path of motion.

Effects of a rotating Sun on AEPs As the sail attitude is referenced to the direction of the Sun, the acceleration provided by the sail is necessarily dependent on the position of the Sun as the asteroid rotates around its own principal axis. As such, it is reasonable to assume that there is an additional effect on the position of the AEPs. At the performance level of $a_c = 0.20$ mm/s^2, only one AEP remains, AEP_3. Figure 5 shows the variation in position of AEP_3, for several different sail attitudes, during one complete rotation of the asteroid. The red diamond represents the initial and final positions. The initial and final positions are equal as the Sun returns to its initial position relative to the asteroid. It should be noted that the locus of points do not represent a feasible trajectory for a spacecraft to follow, but distinct, instantaneous equilibria which are defined only with zero-velocity at that point.

Figure 6 shows the changing eigenvalues of AEP_3 for each set of sail attitudes in Fig. 5. These show the transition in stability characteristics, referenced to those listed in Table 1. The black circles represent the initial eigenvalues and the black crosses represent the final eigenvalues. Most of the AEPs remain unstable throughout the asteroid rotation. However, there are examples, as shown in Figs 6c to 6f, of the AEPs transitioning briefly to linearly stable points of case 1.

.

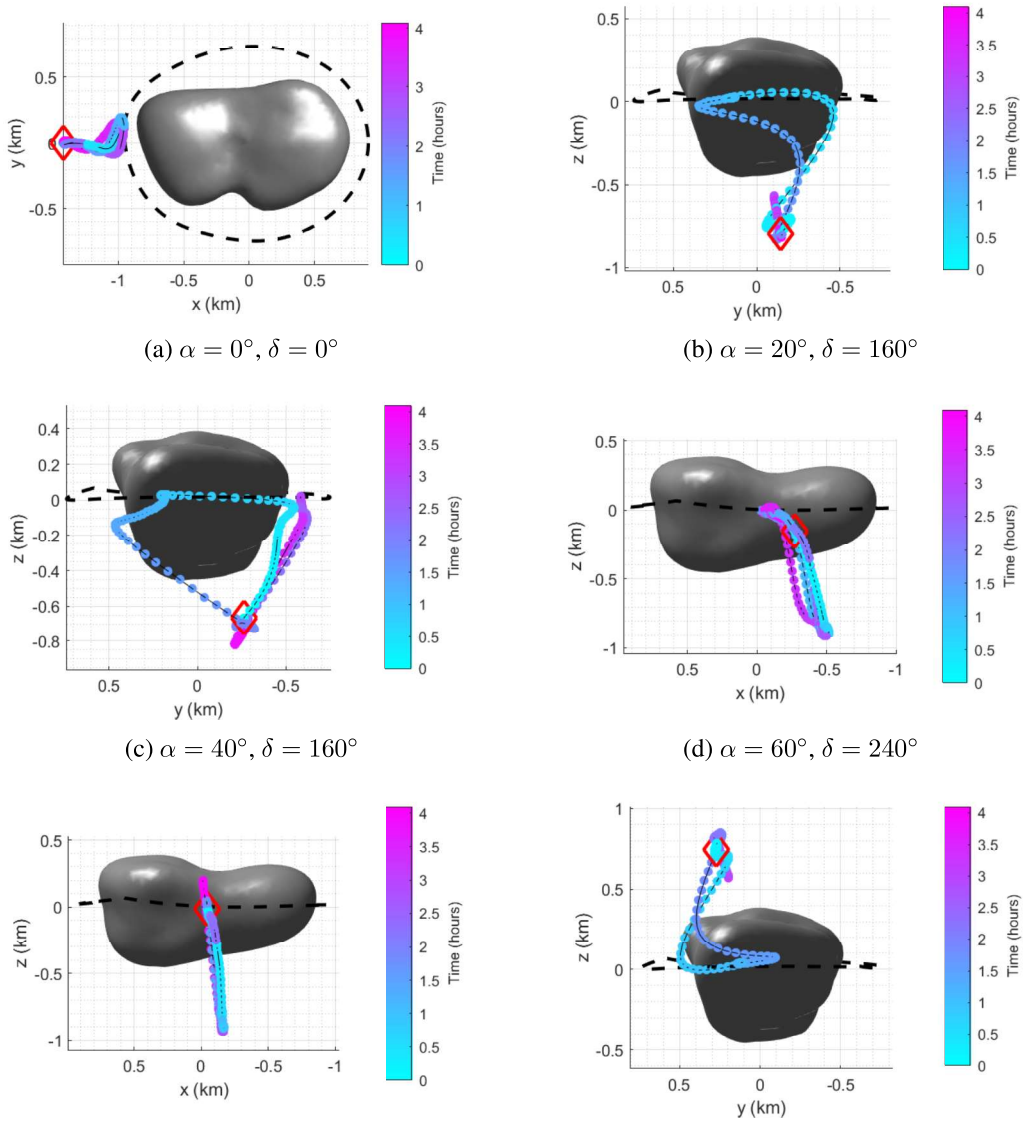

(a) $\alpha = 0°$, $\delta = 0°$

(b) $\alpha = 20°$, $\delta = 160°$

(c) $\alpha = 40°$, $\delta = 160°$

(d) $\alpha = 60°$, $\delta = 240°$

(e) $\alpha = 80°$, $\delta = 240°$

(f) $\alpha = 20°$, $\delta = 320°$

Figure 5: Selection of trajectories for AEP_3 with $a_c = 0.20$ mm/s^2 during one complete rotation of the asteroid for varying values of α and δ. The red diamond marks the AEP at t_0.

Effects of sail performance on the potential ridge line

Application of the solar sail also has an effect on the size, and eventual existence, of the potential ridge line. The ridge line is only defined while the asteroid has its full compliment of equilibrium points. As such, when the performance of the sail reaches such a point that the equilibria begin to disappear, the ridge line is also lost. Figure 7 shows the contraction of the ridge line as a_c increases up to the critical point, the point at which AEP_1 and AEP_2 disappear, which is approximately at $a_c = 0.06$ mm/s^2 and at the initial time point, t_0.

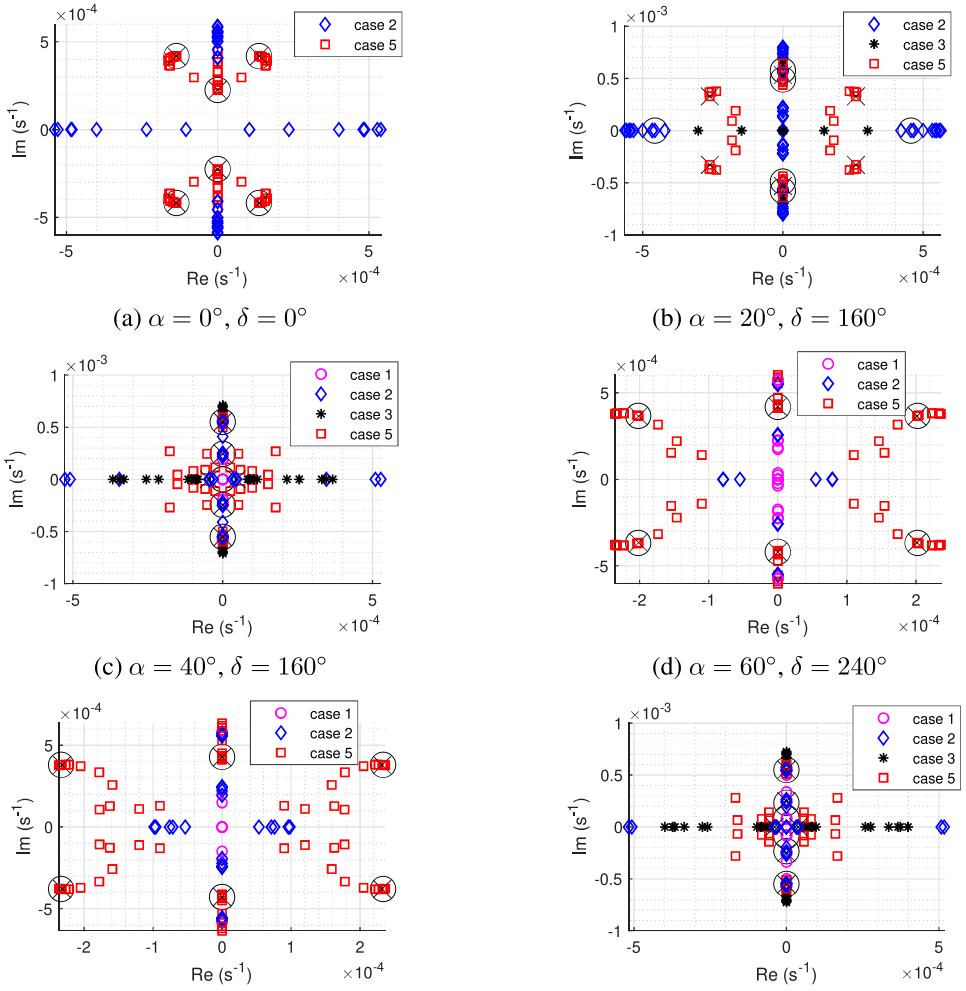

(a) $\alpha = 0°, \delta = 0°$

(b) $\alpha = 20°, \delta = 160°$

(c) $\alpha = 40°, \delta = 160°$

(d) $\alpha = 60°, \delta = 240°$

(e) $\alpha = 80°, \delta = 240°$

(f) $\alpha = 20°, \delta = 320°$

Figure 6: Eigenvalues during rotation of the asteroid for trajectories shown in Fig 5

CHANGING DYNAMICS AT THE POINT OF LANDER SEPARATION

The proposed spacecraft for this work will carry a lander similar to MASCOT, used in the Hayabusa2 mission. The physical parameters of the MASCOT lander are presented in Table 4.[29]

The lander will be carried by a 12U cubesat with standard parameters[30] listed in Table 4. The selection of the 12U model allows for sufficient capacity for storage of the sail as well as the required payloads for relaying the data from the MASCOT lander and surveying the asteroid.

As the performance of the sail is dependent on the mass to area ratio of the sail and complete spacecraft and lander, an iterative method is required to calculate the required sail area for the stated value of a_c. In order to calculate the required size of the sail and the mass of its materials and structure, Newton's method is used. The areal density of the sail structure and materials is taken[31] as $\rho_A = 10$ g/m^2. The full sail and spacecraft parameters are listed in Table 5. Upon release of the lander, the sail performance changes instantaneously, given the new area-to-mass ratio. Table 6

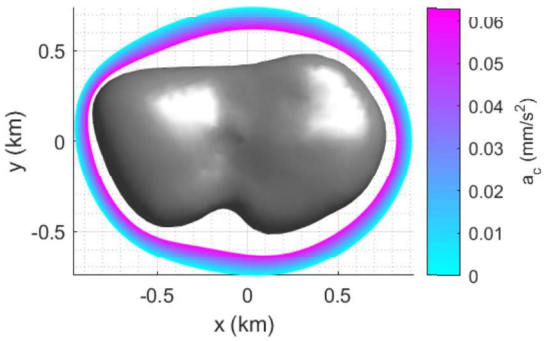

Figure 7: Variation in the potential ridge line for changing sail characteristic acceleration, $a_c \in [0, 0.06]$ mm/s^2

Table 4: Physical parameters of the MASCOT lander[29] and a 12U CubeSat[30]

	MASCOT	12U CubeSat
Mass	13 kg	24 kg
Length	28 cm	23 cm
Depth	29 cm	24 cm
Height	21 cm	36 cm

shows the pre- and post-separation performance values for the sail. With this changing performance, there is also an instantaneous change in the dynamics of the system. Figure 8 shows the changing geometry of the ZVCs in the potential field of Castalia, where Eq. 16 provides the expression for the total effective potential of the system. The two circles represent the only AEP at these levels of a_c. The smaller circle is the AEP for the lower performance, the larger circle for the higher performance.

Table 5: Physical parameters of sail and spacecraft

Spacecraft bus mass	24 kg
MASCOT lander mass	13 kg
Sail mass	10.39kg
Sail areal density (ρ_A)	10 g/m^2
Sail Area	1039.30 m^2
Square sail side length	32.24 m

The change in dynamics brought about by the changing performance of the sail is considerable. Where there was direct access to the surface from the AEP at $a_c = 0.20$ mm/s^2, this is not the case for $a_c = 0.28$ mm/s^2. It would be necessary to either provide a propulsive manoeuvre, or wait for the asteroid to rotate such that the Sun-sail line moves the AEP closer to the surface.

Table 6: Pre- and post-separation parameters for sail and carrier spacecraft combination

	Pre-separation	Post-separation
Total mass	47.39 kg	34.39 kg
Sail Area	1039.30 m^2	1039.30 m^2
a_c	0.20 mm/s^2	0.28 mm/s^2

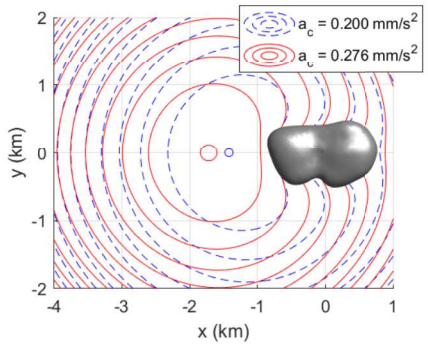

Figure 8: Changing geometry of the Zero Velocity Curves for $a_c = 0.20$ mm/s^2 and $a_c = 0.28$ mm/s^2, with $\alpha = \delta = 0°$. The two circles represent the only AEP at these levels of a_c. The smaller circle is the AEP for the lower performance, the larger circle for the higher performance.

ZERO-VELOCITY DEPLOYMENT OF BALLISTIC LANDERS

The aim of this section is to establish a reliable strategy for the successful deployment of a lander to the surface of the asteroid. In order to do so, a deployment region is sought where the ballistic trajectory will have the best chance of a successful descent. The trajectories presented in this section will be for landers which are released with zero velocity. Once the lander is released from the sail, it no longer experiences the same constant acceleration from SRP and so its dynamics revert to the natural dynamics of the asteroid potential field and this allows separation.

The results in this section will also detail the landing velocity, v_L, and the time of flight, TOF. The importance of presenting the landing velocity is to give some measure of the likelihood of the lander to remain on the surface after touchdown. An excessive landing velocity, and any subsequent bouncing, could lead to the lander escaping the weak gravity field of the asteroid. The escape velocity of 4769 Castalia is approximately $v_{esc} = 0.52$ m/s.

No consideration is made to the lander bouncing, or potential escape thereafter, and a successful lander deployment is defined as one which ends with one successful intersection with the asteroid surface. The success is given by the success rate, which is the ratio of trajectories with a successful intersection with the surface to the total trajectories simulated.

Deployment from equilibrium points

The natural equilibrium points provide a convenient location for lander deployment as they are also useful as hover points for the carrier spacecraft. The carrier acts as a communication relay for the lander and so being in continuous line-of-sight, as is possible from an equilibrium point, is useful. Being placed on the natural potential ridge line also provides easier access to the natural

external region where the AEPs are often located. As the equilibrium points around asteroid Castalia are unstable, they will eventually drift from the equilibrium points. Figure 9 shows the deployment trajectories from each of the four equilibrium points at Castalia.

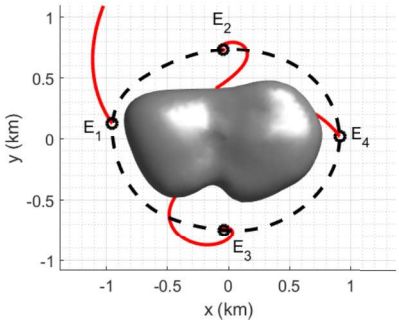

Figure 9: Deployment of lander with zero initial velocity from natural equilibrium points

All but one of the deployments eventually intersects the surface of the asteroid. Deployment from E_1 quickly drifts from the equilibrium point into the exterior region and eventually escaping the asteroid gravity field. From E_4, the lander drifts into the interior region and intersects the asteroid surface. Deployment from points E_2 and E_3 takes a considerably longer time to drift from the equilibrium points. Initially they drift into the exterior region, though retrograde to the asteroids rotation, and this results in the trajectory being pulled back across the potential ridge and put on an impact trajectory. Table 7 shows the landing velocity, v_L, and time of flight, TOF, for each trajectory which reaches the asteroid surface.

Table 7: Landing velocities and time of flight for trajectories from zero velocity deployment

	E_1	E_2	E_3	E_4
v_L (m/s)	-	0.25	0.22	0.14
TOF (hrs)	-	8.84	7.01	4.50

Deployment from the potential ridge line

In this section, 1326 simulations of lander trajectories deployed from the potential ridge line are presented. Deployment from any point along the potential ridge line, with zero initial velocity, brings a 53.77% success rate. Figure 10 shows the results from analysis for 1326 points uniformly spaced along the ridge line.

This shows two distinct regions, with some symmetry, where successful deployment to the surface is indeed possible. The time of flight from this region is still mostly short, with the landing velocities still within an acceptable range.

Deployment internal to the ridge line

It is intuitive to assume that the most successful region for deployment of the lander would be the region interior to the potential ridge line, and this is indeed the case. Figure 11 shows the analysis of

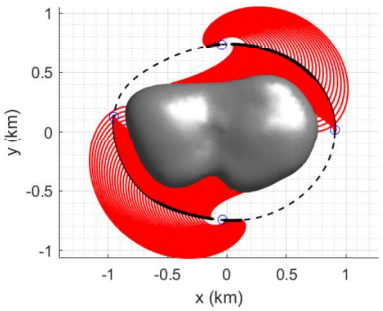

(a) All trajectories which intersect the surface of the asteroid.

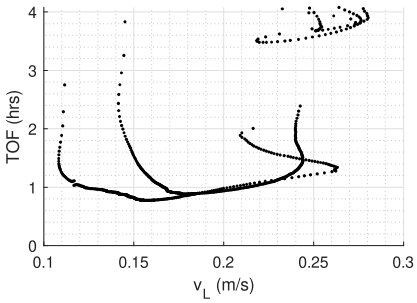

(b) Landing velocity, v_L, and the time of flight, TOF.

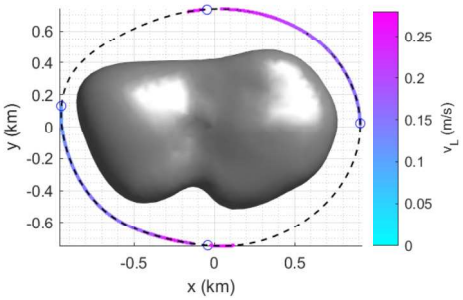

(c) Landing velocity for each deployment location

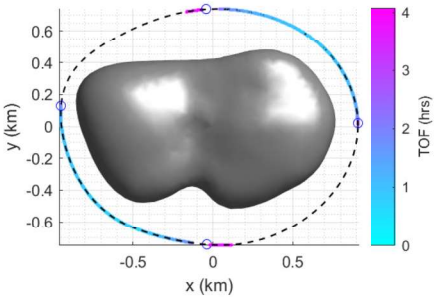

(d) TOF for each deployment location

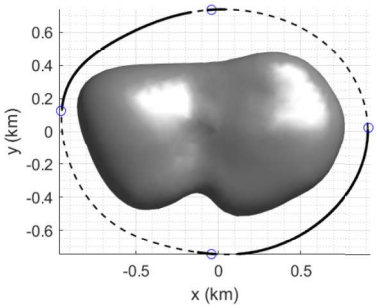

(e) Location of points from which zero velocity release results in escaping trajectory

Figure 10: Monte Carlo analysis of success rates for deployment from the potential ridge line.

trajectories from 1327 deployments in this region. The rate of successful deployment to the surface in this region is 92.01%.

The landing velocities remain within the same range as those for trajectories from the ridge line, though the TOFs are generally, as expected, lower. When the region of unsuccessful trajectories is examined, once again there are two distinct regions, mirrored on the opposite side of the asteroid, and are in the same area as the unsuccessful ridge line trajectories.

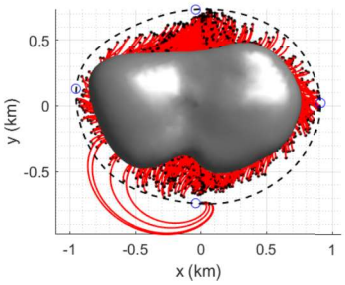

(a) All trajectories which intersect the surface of the asteroid.

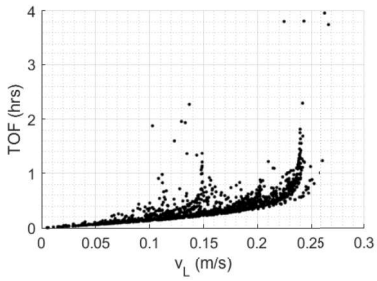

(b) Landing velocity, v_L, and the time of flight, TOF.

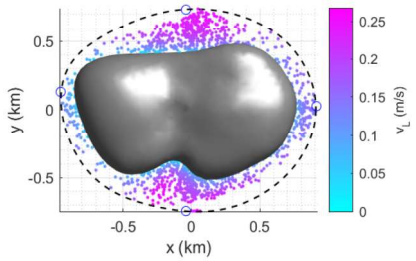

(c) Landing velocity for each deployment location

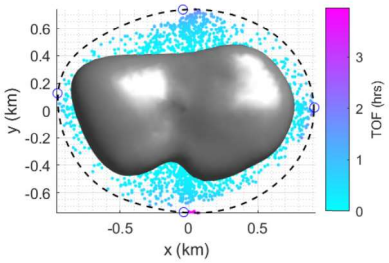

(d) TOF for each deployment location

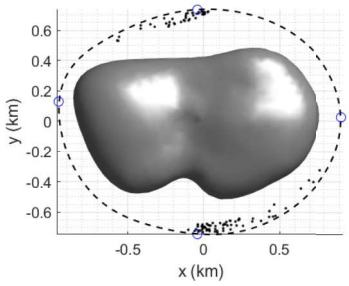

(e) Location of points from which zero velocity release results in escaping trajectory

Figure 11: Monte Carlo analysis of success rates for deployment from the interior region to the ridge line.

Deployment external to the ridge line

When the spacecraft is in the region external to the ridge line, the lander has an added challenge in reaching the asteroid surface. Figure 12 shows the analysis of deployment from this region.

This simulation contains 1326 randomly chosen distinct points which lie between the ridge line and another line which follows the ridge line but at twice the distance from the asteroid centre. As is expected, the vast majority of ballistic deployments in this region do not reach the surface, with only a 4.15% success rate. However, there are two regions close to the ridge line which do offer the potential for descent to the surface. These regions are separated symmetrically as with those of the previous regions, and they are in the same area as the successful ridge line trajectories.

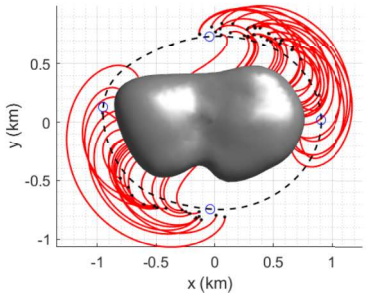

(a) All trajectories which intersect the surface of the asteroid.

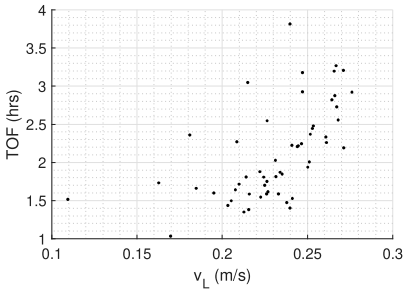

(b) Landing velocity, v_L, and the time of flight, TOF.

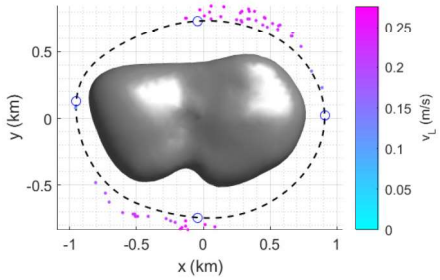

(c) Landing velocity for each deployment location

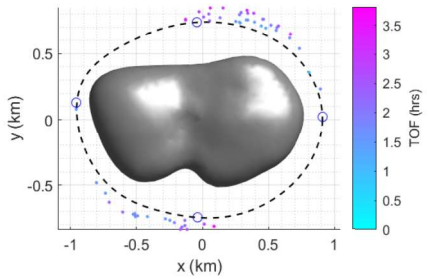

(d) TOF for each deployment location

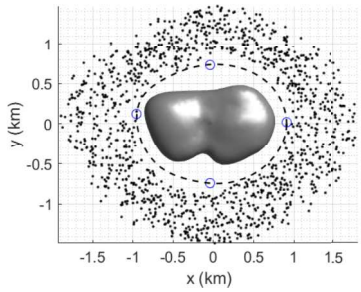

(e) Location of points from which zero-velocity release results in escaping trajectories

Figure 12: Monte Carlo analysis of success rates for deployment from the exterior to the potential ridge line.

CONCLUSIONS

This work has presented the dynamics in near-asteroid space with the inclusion of a solar sail. The sail performance and attitude, as well as the position of the Sun relative to the asteroid, are all seen to play an important role in the time varying dynamics of this complex regime. A study shows the changing dynamics as the sail attitude and performance, and solar position, vary. Examples are given of the changes in AEP position and stability, through one full rotation of the asteroid.

The work also presented a probabilistic analysis of successful intersection with the surface of a lander after ballistic deployment with zero initial velocity in four distinct regions in the phase

space: natural equilibrium points, along the potential ridge line, interior to the potential ridge line and exterior to the potential ridge line. Unsurprisingly, the interior region provided the highest success rate (92.01%) for the lander to successfully make its way to the surface of the asteroid. This means that any deployment strategy that aims to deliver a ballistic lander to the surface would be best placed to do so by deploying from this region. It is, however, still possible to achieve a successful ballistic deployment from outside the potential ridge line if a small impulse can be given to the lander at release.

ACKNOWLEDGEMENTS

Colin McInnes was supported by a Royal Academy of Engineering Chair in Emerging Technologies. Iain Moore was supported by the Engineering and Physical Sciences Research Council (EPSRC).

REFERENCES

[1] M. Vergaaij, C. R. McInnes, and M. Ceriotti, "Economic assessment of high-thrust and solar-sail propulsion for near-earth asteroid mining," *Advances in Space Research*, jun 2020, 10.1016/j.asr.2020.06.012.

[2] C. Lange, J. Biele, S. Ulamec, C. Krause, B. Cozzoni, O. Küchemann, S. Tardivel, T.-M. Ho, C. Grimm, J. T. Grundmann, E. Wejmo, S. Schröder, M. Lange, J. Reill, A. Hérique, Y. Rogez, D. Plettemeier, I. Carnelli, A. Galvez, C. Philippe, M. Küppers, B. Grieger, J. G. Fernandez, J. Grygorczuk, M. Tokarz, and C. Ziach, "MASCOT2 – A small body lander to investigate the interior of 65803 Didymos/ moon in the frame of the AIDA/AIM mission," *Acta Astronautica*, Vol. 149, aug 2018, pp. 25–34, 10.1016/j.actaastro.2018.05.013.

[3] M. Beckman, K. Berry, B. Sutter, A. May, K. Williams, B. W. Barbee, and B. Williams, "OSIRIS-REx Touch-And-Go (TAG) Mission Design and Analysis," *36th Annual AAS Guidance and Control Conference, Breckenridge, CO, USA*, 2013.

[4] M. Yoshikawa, A. Fujiwara, and J. Kawaguchi, "Hayabusa and its adventure around the tiny asteroid Itokawa," *Proceedings of the International Astronomical Union*, Vol. 2, No. 14, 2007, 10.1017/s174392130701085x.

[5] D. K. Yeomans, "Radio Science Results During the NEAR-Shoemaker Spacecraft Rendezvous with Eros," *Science*, Vol. 289, sep 2000, pp. 2085–2088, 10.1126/science.289.5487.2085.

[6] K.-H. Glassmeier, H. Boehnhardt, D. Koschny, E. Kührt, and I. Richter, "The Rosetta Mission: Flying Towards the Origin of the Solar System," *Space Science Reviews*, Vol. 128, jan 2007, pp. 1–21, 10.1007/s11214-006-9140-8.

[7] M. Leslie, J. Les, K. Pater, C.-R. Julie, and F. Andreas, *Near-Earth Asteroid (NEA) Scout*. SPACE Conferences and Exposition, American Institute of Aeronautics and Astronautics, 2014, 10.2514/6.2014-4435.

[8] A. Farrés, S. Soldini, and Y. Tsuda, "JAXA's Trojan Asteroids Mission: Trajectory Design of theSolar Power Sail and its Lander," *International Symposium on Solar Sailing 2017*, Kyoto, Japan, 2017.

[9] X. Zeng, S. Gong, J. Li, and K. T. Alfriend, "Solar Sail Body-Fixed Hovering over Elongated Asteroids," *Journal of Guidance, Control, and Dynamics*, Vol. 39, jun 2016, pp. 1223–1231, 10.2514/1.g001061.

[10] A. D'Ambrosio, C. Circi, and X. Zeng, "Solar-photon sail hovering orbits about single and binary asteroids," *Advances in Space Research*, Vol. 63, jun 2019, pp. 3691–3705, 10.1016/j.asr.2019.02.021.

[11] Y. Jiang, H. Baoyin, J. Li, and H. Li, "Orbits and manifolds near the equilibrium points around a rotating asteroid," *Astrophysics and Space Science*, Vol. 349, sep 2013, pp. 83–106, 10.1007/s10509-013-1618-8.

[12] Y. Jiang, H. Baoyin, X. Wang, Y. Yu, H. Li, C. Peng, and Z. Zhang, "Order and chaos near equilibrium points in the potential of rotating highly irregular-shaped celestial bodies," *Nonlinear Dynamics*, Vol. 83, aug 2015, pp. 231–252, 10.1007/s11071-015-2322-8.

[13] Y. Jiang, Y. Yu, and H. Baoyin, "Topological classifications and bifurcations of periodic orbits in the potential field of highly irregular-shaped celestial bodies," *Nonlinear Dynamics*, Vol. 81, feb 2015, pp. 119–140, 10.1007/s11071-015-1977-5.

[14] Y. Jiang and H. Baoyin, "Periodic orbit families in the gravitational field of irregular-shaped bodies," *The Astronomical Journal*, Vol. 152, oct 2016, p. 137, 10.3847/0004-6256/152/5/137.

[15] Y. Jiang, H. Baoyin, X. Wang, and H. Li, "Stability and motion around equilibrium points in the rotating plane-symmetric potential field," *Results in Physics*, Vol. 10, sep 2018, pp. 487–497, 10.1016/j.rinp.2018.06.056.

[16] Y. Jiang and H. Baoyin, "Periodic orbits related to the equilibrium points in the potential of Irregular-shaped minor celestial bodies," *Results in Physics*, Vol. 12, 2019, pp. 368–374, 10.1016/j.rinp.2018.11.049.

[17] H. Yang, X. Bai, and S. Li, "Artificial Equilibrium Points near Irregular-Shaped Asteroids with Continuous Thrust," *Journal of Guidance, Control, and Dynamics*, Vol. 41, jun 2018, pp. 1308–1319, 10.2514/1.g003295.

[18] A. Peloni, M. Ceriotti, and B. Dachwald, "Solar sail trajectory design for a multiple near-Earth asteroid rendezvous mission," *Journal of Guidance, Control, and Dynamics*, Vol. 39, No. 12, 2016, pp. 2712–2724, 10.2514/1.G000470.

[19] S. Tardivel, D. J. Scheeres, P. Michel, S. V. wal, and P. Sánchez, "Contact Motion on Surface of Asteroid," *Journal of Spacecraft and Rockets*, Vol. 51, nov 2014, pp. 1857–1871, 10.2514/1.a32939.

[20] D. J. Scheeres, *Orbital Motion in Strongly Perturbed Environments*. Springer, 2012.

[21] F. F. P. Rossi, A; Marzari, "Orbital Evolution Around Irregular Bodies," *Earth Planets Space*, Vol. 51, 1999, pp. 1173–1180.

[22] A. Viale, C. McInnes, and M. Ceriotti, "Dynamics of a Nonrigid Orbital Siphon at a Near-Earth Asteroid," *Journal of Guidance, Control, and Dynamics*, jul 2020, pp. 1–15, 10.2514/1.g004894.

[23] D. J. Scheeres, S. J. Ostro, R. S. Hudson, and R. A. Werner, "Orbits Close to Asteroid 4769 Castalia," *Icarus*, Vol. 121, No. 1, 1996, pp. 67–87, 10.1006/icar.1996.0072.

[24] X. Wang, J. Li, and S. Gong, "Bifurcation of equilibrium points in the potential field of asteroid 101955 Bennu," *Monthly Notices of the Royal Astronomical Society*, Vol. 455, dec 2015, pp. 3724–3734, 10.1093/mnras/stv2426.

[25] S. Tardivel and D. J. Scheeres, "Ballistic Deployment of Science Packages on Binary Asteroids," *Journal of Guidance, Control, and Dynamics*, Vol. 36, may 2013, pp. 700–709, 10.2514/1.59106.

[26] S. Tardivel, *The Deployment of Scientific Packages to Asteroid Surfaces*. PhD thesis, University of Colorado, 2014.

[27] C. R. McInnes, *Solar Sailing: Technology, Dynamics and Mission Applications*. Chichester: Springer-Praxis, 1999.

[28] J. Simo and C. R. McInnes, "Solar sail orbits at the Earth–Moon libration points," *Communications in Nonlinear Science and Numerical Simulation*, Vol. 14, dec 2009, pp. 4191–4196, 10.1016/j.cnsns.2009.03.032.

[29] F. Scholten, F. Preusker, S. Elgner, K.-D. Matz, R. Jaumann, J. Biele, D. Hercik, H.-U. Auster, M. Hamm, M. Grott, C. Grimm, T.-M. Ho, A. Koncz, N. Schmitz, F. Trauthan, S. Kameda, S. Sugita, R. Honda, T. Morota, E. Tatsumi, Y. Cho, K. Yoshioka, H. Sawada, Y. Yokota, N. Sakatani, M. Hayakawa, M. Matsuoka, M. Yamada, T. Kouyama, H. Suzuki, C. Honda, and K. Ogawa, "The descent and bouncing path of the Hayabusa2 lander MASCOT at asteroid (162173) Ryugu," *Astronomy & Astrophysics*, Vol. 632, dec 2019, p. L3, 10.1051/0004-6361/201936757.

[30] R. Hevner, W. Holemans, J. Puig-Suari, and R. Twiggs, "An Advanced Standard for CubeSat," *Proceedings of the 25th Annual AIAA/USU Conference on Small Satellites*, Logan, UT, USA, 2011.

[31] M. Ceriotti and C. R. McInnes, "Natural and sail-displaced doubly-symmetric Lagrange point orbits for polar coverage," *Celestial Mechanics and Dynamical Astronomy*, Vol. 114, No. 1-2, 2012, pp. 151–180, 10.1007/s10569-012-9422-2.